Journal of Structural Biology xxx (2012) xxx–xxx

Contents lists available at SciVerse ScienceDirect

Journal of Structural Biology

journal homepage: www.elsevier.com/locate/yjsbi

# Image formation in cellular X-ray microscopy

Joaquin Oton [a], C.O.S. Sorzano [a], Eva Pereiro [b], Jesús Cuenca-Alba [a], Rafael Navarro [c], Jose M. Carazo [a], Roberto Marabini [d,*]

[a] Centro Nacional de Biotecnología, Ciudad Universitaria de Cantoblanco, Calle Darwin, 3, 28049 Madrid, Spain
[b] MISTRAL Beamline – Experiments Division, ALBA Synchrotron Light Source, BP 1413, Km. 3.3 Carretera de Cerdanyola del Vallés a Sant Cugat del Vallés, 08290 Cerdanyola del Vallés, Barcelona, Spain
[c] ICMA, CSIC-Universidad de Zaragoza, Facultad de Ciencias-c, Pedro Cerbuna 12, 50009 Zaragoza, Spain
[d] Escuela Politécnica Superior, Ciudad Universitaria de Cantoblanco, Calle Francisco Tomás y Valiente, 11, 28049 Madrid, Spain

ARTICLE INFO

*Article history:*
Received 4 October 2011
Received in revised form 4 January 2012
Accepted 5 January 2012
Available online xxxx

*Keywords:*
X-ray microscopy
3D reconstruction
Point spread function
Image formation model

ABSTRACT

*Soft X-ray Tomographic* (TomoX) microscopy has become a reality in the last years. The resolution range of this technique nicely fits between confocal and electron microscopies and will play a key role in the elucidation of the organization between the molecular and the organelle levels. In fact, it offers the possibility of imaging three-dimensional structures of hydrated biological specimens near their native state without chemical pre-treatment. Ideally, TomoX reconstructs the specimen absorption coefficients from projections of this specimen, but, unfortunately, X-ray micrographs are only an approximation to projections of the specimen, resulting in inaccuracies if a tomographic reconstruction is performed without explicitly incorporating these approximations. In an attempt to mitigate some of these inaccuracies, we develop in this work an image formation model within the approximation of assuming incoherent illumination.



## 1. Introduction

Structural biology aims at the visualization of microscopic biological structures with the ultimate goal of understanding the molecular mechanisms taking place in the healthy as well as in the pathological cell. In the last decade a new microscopy technique has emerged, a technique able to visualize whole cells in cryo conditions with a resolution between 50 and 15 nm. This is the field of *Cellular Soft X-ray Tomography* (TomoX) (Schneider, 1998). Many studies so far have presented 3D reconstructions generated by X-ray microscopy (Weiss et al., 2000a; Thieme et al., 2003; Larabell and Le Gros, 2004; Le Gros et al., 2005; Gu et al., 2007; Parkinson et al., 2008; Uchida et al., 2009; Carrascosa et al., 2009; Hanssen et al., 2011). In most cases, the data have been processed using software developed for electron microscopy (EM) data (as can be SPIDER (Frank et al., 1996) or IMOD (Kremer et al., 1996)) without considering the particularities of the new microscope. Obviously, this is a suboptimum situation, and still better results would be obtained should an accurate TomoX image formation model were embedded within the 3D reconstruction process. The main purpose of this article is to start investigating this issue, presenting a first development in which we describe the image formation process within the simplification of assuming incoherent illumination. However, and still within its approximation, this modeling work opens the door to the design of new 3D reconstruction algorithms that explicitly incorporate the image model within the reconstruction algorithm.

Clearly, image processing for TomoX data should be rather different from the EM case, since TomoX images have larger contrast and are less noisy than EM ones. Moreover, the data collection geometry (usually single-tilt axis) helps to reduce the space of possible solutions. Unfortunately, TomoX images are, in general, a poorer approximation to ideal projection images than EM ones. Therefore, in this field the image processing challenge is not the one of fighting the poor signal-to-noise ratio as in EM, but that of the characterization of the microscope PSF and its appropriate incorporation into 3D reconstruction methods. As in any other microscopy, the objective in the X-ray microscope acts as a low-pass spatial frequency filter. Therefore, the PSF of the zone plate objective has to be taken into account. Weiss et al. (2000b) presented PSF calculations for realistic X-ray objectives assuming that the whole specimen is in focus.

## 2. Theoretical background

In this section we discuss the physical principles in which X-ray microscopy is based. First, the interaction of X-ray and matter is introduced and then the image formation process for an ideal microscope is presented for the incoherent case.

* Corresponding author. Fax: +34 91 497 2235.
*E-mail address:* roberto@cnb.uam.es (R. Marabini).

1047-8477/$ - see front matter © 2012 Elsevier Inc. All rights reserved.
doi:10.1016/j.jsb.2012.01.006

### 2.1. Interaction of soft X-ray with mater in the water window

To fully understand the possibilities and limitations of X-ray microscopy, we need to consider how X-ray photons (in the range of 284–543 eV) interact with matter. Readers interested in the details of X-ray matter interaction may find more information in Kirz et al. (1995)and Howells et al. (2007). For the purpose of this work, suffices to say that absorption contrast at those energies has been found experimentally sufficient to image cellular details in the resolution range of 20–50 nm, so that most works in this field only use absorption contrast. We will, therefore, concentrate in the following only in this effect. Under these circumstances, the Beer–Lambert law relates the absorption of light to the properties of the material through which the light is traveling:

$$\frac{dI(z)}{dz} = -\mu I(z) \tag{1}$$

where $\mu$ is the absorption coefficient, $I(z)$ is the light intensity at plane $z$ assuming the light travels parallel to the $z$ axis. In purity, Beer–Lambert law is only valid under certain limited conditions: the light entering the medium must be perfectly collimated, and the medium itself must be uniformly absorbing. Nevertheless, when scattering effects may be neglected, an extended Beer–Lambert law is often used to describe the light attenuation inside typical specimens (Howells et al., 2007):

$$\frac{dI(x,y,z)}{dz} = -\mu(x,y,z)I(x,y,z) \tag{2}$$

An interesting property of soft X-rays is the so called *water window* for photon energies between the K-absorption edges of carbon (284 eV) and oxygen (543 eV) (Wolter, 1952). Most biological microscopy studies are done in this window because water (oxygen) is relatively transparent to these X-ray range while protein (carbon) and other elements found in biological specimens are much more absorbing. Therefore, it is possible to visualize hydrated biological specimens near their native state without chemical staining. For example, working at 500 eV an ice block of 7.5 μm of thickness will block 60% of the incident photons, the same effect may be obtained using a protein block of 0.54 μm (equations involved in these calculations are available at Howells et al. (2007)).

### 2.2. Image formation theory in X-ray microscopy

Conceptually, a transmission X-ray microscope is a simple device formed by: a light source, a condenser lens that focuses the incident light onto the specimen and an objective lens that produces the image. X-rays do not refract easily, so X-rays microscopes use either Fresnel zone plates or elliptical mirrors to focus light (mirrors are only used as condenser lens). A detailed description of the different types of X-ray microscopes is available at Howells et al. (2007) Section 3. We just remark here that for X-ray tomography and thick specimens the microscope limited depth of focus plays an important role.

In the standard water-window X-ray microscopy, the contrast produced by differences in light absorption between different structures is the one currently used to produce the images. Alternative sources of contrast, such as phase-contrast, have also been investigated (see e.g. Schmahl and Rudolph (1987), Rudolph et al. (1990), Jacobsen (1992)). *A priori*, this is an interesting approach since as the energy increases, phase contrast becomes dominant and depth of focus increases. Nevertheless, the relationship between phase shifts and absorption coefficient needs to be further investigated – specially for those cases in which the phase differences are enhanced using Zernike-type phase contrast microscopes – because the relation between phase-shifts and absorption coefficients may be non linear.

In a first order approximation, there is an agreement to model X-ray microscopes as systems formed by a single ideal lens illuminated by a parallel wave (Weiss et al., 2000b). Therefore, within this

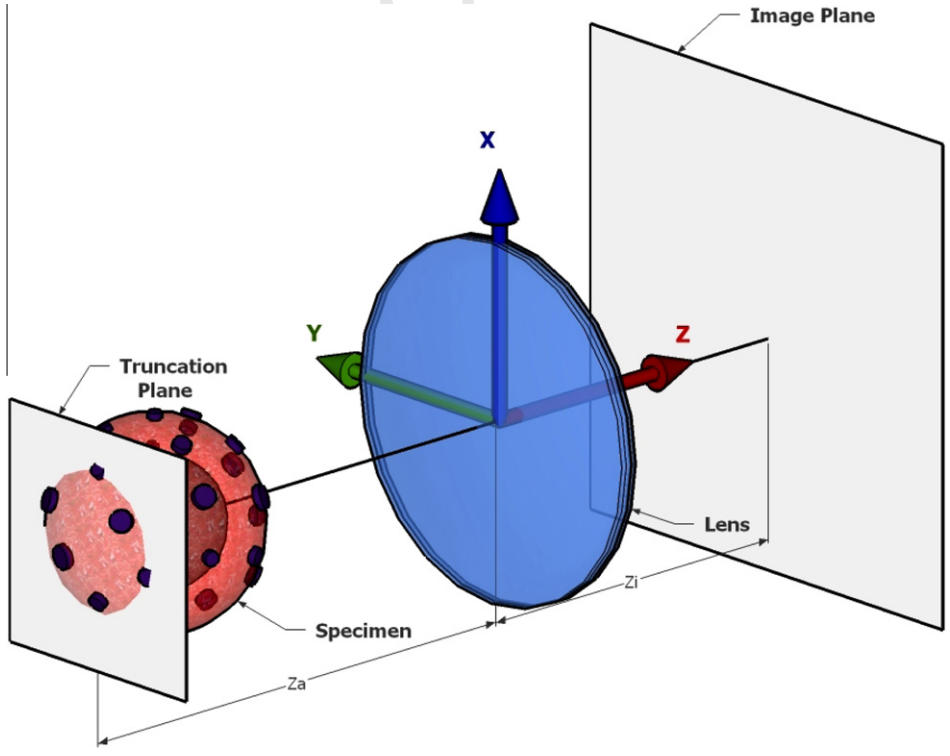


**Fig. 1.** Schematic representation of an X-ray microscope where the relevant coordinates of the optical system are shown. The coordinate system origin is at the lens center and it is represented by green ($x$), blue ($y$) and red ($z$) arrows.

Q1 Please cite this article in press as: Oton, J., et al. Image formation in cellular X-ray microscopy. J. Struct. Biol. (2012), doi:10.1016/j.jsb.2012.01.006

approximation, the only source of aberrations is the limited size of the lens. Because the microscope imaging system collects only a fraction of the light emitted by a given point, it cannot focus the light into a perfect three-dimensional image of the point. Instead, the point appears widened and spread into a three-dimensional blob known as point spread function (PSF). The PSF of an ideal lens is well known (see Mielenz (1999), Weiss et al. (2000b)). If the specimen is a 2D dimensional object (that is, thinner than the lens depth of focus), it is straightforward to relate absorption coefficients in the specimen with measured intensities (see Attwood (2007) Chapter 9 for details). However, for thick specimens, X-ray microscopes produce images of the object that are not geometrical projections, or what is the same: absorption coefficients and recorded images are no longer linearly related. In this situation the image formation model needs to be introduced in the reconstruction algorithm if accurate reconstructions are desired.

### 2.3. Image formation model for thick specimens

In this work, and as a first approximation, we study the image formation process of a thick 3D semitransparent object lit with incoherent light when observed by an X-ray microscope. It should be noted that currently there are three cellular biology oriented X-ray microscopes in operation or at commissioning at ALBA (Barcelona), Bessy II (Berlin) and ALS (San Francisco), each of them with a different design and, certainly, for each of them the approximations considered in this work may be more or less applicable. The microscope at ALBA in its current implementation is probably the one operating under considerations closer to the ones considered here, while the one at Bessy II works under partial coherent illumination (Schneider et al., 2010).

So far we have introduced the microscope PSF and how the intensity decays as it goes through the specimen, but we have not coupled both effects together. Before describing our derivation, we should mention that a similar problem has been solved for fluorescent microscopy (Agard et al., 1989) and for the 2D case in X-ray microscopy (Weiss et al., 2000a; von Hofsten et al., 2007). To the best of our knowledge, the only works that we have been able to find for the 3D case are those in which numerical modeling (instead of analytical derivation) is used (see Bertilson et al. (2011)) or in Dey et al. (2002), where some results are presented without derivation. Furthermore, we disagree with the solution proposed in this latter work, especially in the areas describing the influence of the PSF in the different specimen planes.

In the following we derive the relationship between the image recorded in the microscope CCD and the object absorption coefficients for thick objects. The derivation starts with Eq. (3), that relates the electromagnetic fields at two planes $z = z_i$ and $z = z_a$ in absence of any specimen. $z_i$ and $z_a$ define the planes in which the image is recorded and a plane before the lens, respectively. This equation may be found in many optical textbooks (see Goodman (1996) Chapter 5).

$$\begin{aligned} U^{z_i}(x,y) &= U_g^{z_i}(x,y,z_a) \underset{x,y}{\otimes} \tilde{h}(x,y,D(z_a,z_i)) \quad \tilde{h}(x,y,D(z_a,z_i)) \\ &= \exp\{jk(z_a+z_i)\} \\ &\quad \times \mathscr{F}\left\{P(x\lambda z_i, y\lambda z_i)\exp\left\{\frac{jk}{2}(x^2+y^2)(\lambda z_i)^2 D(z_a,z_i)\right\}\right\} \end{aligned} \tag{3}$$

where $U^{z_i}(x,y)$ is the electric field measured at the CCD plane, $U_g^{z_i}(x,y,z_a) \equiv \frac{1}{M}U^{z_i}\left(\frac{x}{M},\frac{y}{M},z_a\right)$ is the field that would have been measured at the CCD plane if we have had an ideal and infinite lens ($M$ is the geometric magnification of the optical system), $j \equiv \sqrt{-1}$. Note that it is not assumed that the plane $z_i$ is in focus, that is, the equation remains valid even if the recording device is out of focus. $k$ is the wave function, that is, $\frac{2\pi}{\lambda}$, $\lambda$ is the wavelength, $\mathscr{F}$ the Fourier transform and $D(z_a,z_i) \equiv \frac{1}{z_a}+\frac{1}{z_i}-f$. Finally $P$ is the lens aperture and $f$ the focal length.

At this point (see Fig. 1) we place a specimen in the field and redefine $U^{z_i}(x,y,z_a)$ as an auxiliary magnitude that cannot, in general, be measured and gives the image that would be produced by a *truncated* version of the specimen, that is, by a specimen from which all density placed at points with $z > z_a$ had been removed. Under these assumptions, Eq. (3) may be rewritten as:

$$U^{z_i}(x,y,z_a) = U_g^{z_i}(x,y,z_a) \underset{x,y}{\otimes} \tilde{h}(x,y,D(z_a,z_i)) \tag{4}$$

If we assume the specimen is a quasi-isotropic non-magnetic substance, then the field in the outgoing plane of any slice of the specimen can be defined as a function of the field in the incoming plane:

$$U_g^{z_i}(x,y,z_a+\Delta z_a) \simeq (1-\tilde{\mu}(x,y,z_a)\Delta z_a)U_g^{z_i}(x,y,z_a), \tag{5}$$

where $\tilde{\mu}(x,y,z_a) \equiv \tilde{\mu}^R(x,y,z_a) + i\tilde{\mu}^I(x,y,z_a) = \frac{k}{2}(Im(\chi(x,y,z_a)) - iRe(\chi(x,y,z_a)))$ ($\chi$ is the electric susceptibility).

For an electric field amplitude distribution $U(x,y,z_a)$ placed in the backplane $z_a + \Delta z_a$ of a slice, we can calculate the field distribution in the sensor plane $U^{z_i}(x,y,z_a+\Delta z_a)$, substituting Eq. (5) into Eq. (4):

$$\begin{aligned} U^{z_i}(x,y,z_a+\Delta z_a) &= U_g^{z_i}(x,y,z_a+\Delta z_a) \underset{x,y}{\otimes} \tilde{h}(x,y,D(z_a+\Delta z_a,z_i)) \\ &= \left[(1-\tilde{\mu}_g(x,y,z_a)\Delta z)U_g^{z_i}(x,y,z_a)\right] \underset{x,y}{\otimes} \tilde{h}(x,y,D(z_a \\ &\quad +\Delta z_a,z_i)) \end{aligned} \tag{6}$$

where $\tilde{\mu}_g(x,y,z_a) = \tilde{\mu}\left(\frac{x}{M},\frac{y}{M},z_a\right)$.

By definition, in the incoherent case, the intensity measured by the photodetector is

$$I^{z_i}(x,y,z_a+\Delta z_a) = \langle U^{z_i}(x,y,z_a+\Delta z_a)U^{z_i*}(x,y,z_a+\Delta z_a)\rangle \tag{7}$$

where $\langle\rangle$ is the time-averaged operator.

Combining Eqs. (6) and (7) we get:

$$\begin{aligned} I^{z_i}(x,y,z_a+\Delta z_a) &= [|1-\tilde{\mu}_g(x,y,z_a)\Delta z|^2 I_g^{z_i}(x,y,z_a)] \\ &\quad \underset{x,y}{\otimes} |\tilde{h}(x,y,D(z_a+\Delta z,z_i))|^2 \\ &= \left[\left(1-\tilde{\mu}_g^R(x,y,z_a) - i\tilde{\mu}_g^I(x,y,z_a)\Delta z_a\right)\cdot \right. \\ &\quad \left.\left(1-\tilde{\mu}_g^R(x,y,z_a) + i\tilde{\mu}_g^I(x,y,z_a)\Delta z_a\right) I_g^{z_i}(x,y,z_a)\right] \\ &\quad \underset{x,y}{\otimes} |\tilde{h}(x,y,D(z_a+\Delta z_a,z_i))|^2 \\ &= \left(1-2\tilde{\mu}_g^R(x,y,z_a)\Delta z_a + O^2(\tilde{\mu}_g\Delta z)\right) I_g^{z_i}(x,y,z_a) \\ &\quad \underset{x,y}{\otimes} |\tilde{h}(x,y,D(z_a+\Delta z_a,z_i))|^2 \end{aligned} \tag{8}$$

where $O^2(x)$ refers to second order terms. A more detailed derivation of Eq. (8) is available at the Appendix Section.

If we define $\mu \equiv 2\tilde{\mu}_g^R$ and since $O^2(\tilde{\mu}_g\Delta z) \approx 0$ for photons in the water window range:

$$\begin{aligned} I^{z_i}(x,y,z_a+\Delta z) &\approx ((1-\mu(x,y,z_a)\Delta z))I_g^{z_i}(x,y,z_a) \underset{x,y}{\otimes} |\tilde{h}(x,y,D(z_a \\ &\quad +\Delta z,z_i))|^2 \\ &= I_g^{z_i}(x,y,z_a) \underset{x,y}{\otimes} |\tilde{h}(x,y,D(z_a+\Delta z,z_i))|^2 \\ &\quad - \mu(x,y,z_a) I_g^{z_i}(x,y,z_a) \underset{x,y}{\otimes} |\tilde{h}(x,y,D(z_a \\ &\quad +\Delta z,z_i))|^2 \Delta z \end{aligned} \tag{9}$$

If we define $h \equiv \tilde{h}^2$, using Eq. (4) and assuming $\hat{h}$ is a slowly varying function along $z_a$.

$$= I^{z_i}(x,y,z_a) - \mu(x,y,z_a) I_g^{z_i}(x,y,z_a) \underset{x,y}{\otimes} h(x,y,D(z_a + \Delta z_a, z_i))\Delta z_a \quad (10)$$

therefore

$$\frac{I^{z_i}(x,y,z_a+\Delta z_a) - I^{z_i}(x,y,z_a)}{\Delta z_a} = -\mu(x,y,z_a) I_g^{z_i}(x,y,z_a) \underset{x,y}{\otimes} h(x,y,D(z_a + \Delta z_a, z_i))$$

taking limit when $\Delta z_a \to 0$

$$\frac{dI^{z_i}(x,y,z_a)}{dz_a} = -\mu(x,y,z_a) I_g^{z_i}(x,y,z_a) \underset{x,y}{\otimes} h(x,y,D(z_a,z_i)) \quad (11)$$

This equation may be rewritten in integral form:

$$I^{z_i}(x,y,z_A) = I^{z_i}(x,y,z_0) - \int_{z_0}^{z_A} \left(\mu(x,y,z_a) I_g^{z_i}(x,y,z_a)\right) \underset{x,y}{\otimes} h(x,y,D(z_a,z_i))dz_a = I^{z_i}(x,y,z_0) - \int_{z_0}^{z_A} \left(\mu(x,y,z) I_g^{z_i}(x,y,z_0) e^{-\int_{z_0}^{z_a}\mu(x,y,\xi)d\xi}\right) \underset{x,y}{\otimes} h(x,y,D(z_a,z_i))dz_a \quad (12)$$

where $z_0$ is a point before the specimen and $z_A$ is a point after the specimen but before the lens.

Without further assumptions it is difficult to obtain the specimen absorption coefficients ($\mu$) from the experimental data ($I^{z_i}$), even assuming that the microscope point spread function ($h$) can be approximated by the point spread function of an ideal lens. In the following we simplify the above equation for two cases: (i) point spread function is ignored (ii) point spread function is constant along the optical axis (specimen is fully in-focus).

### 2.3.1. Image formation model when the point spread function is ignored

The relationship between the recorded intensity and $\mu$ is rather complex, fortunately, if $h$ may be dropped (i.e. $h$ is a $\delta$), the expression can be simplified using the *Second Fundamental Theorem of Calculus*. The second fundamental theorem of calculus holds for $f$ being a continuous function on an open interval and at any point within the interval, and states that if the function $F(x)$ is defined by the integral $F(x) = \int f(s)ds$ then $\frac{F(x)}{dx} = f(x)$. So, Eq. (12) becomes

$$I^{z_i}(x,y,z_A) = I^{z_i}(x,y,z_0)\left(1 - \int_{z_0}^{z_A}\left(\mu(x,y,z)e^{-\int_{z_0}^{z}\mu(x,y,\xi)d\xi}\right)dz\right) = I^{z_i}(x,y,z_0)\left(1 + \int_{z_0}^{z_A}\left(\frac{d}{dz}e^{-\int_{z_0}^{z}\mu(x,y,\xi)d\xi}\right)dz\right) = I^{z_i}(x,y,z_0)\left(e^{-\int_{z_0}^{z_A}\mu(x,y,\xi)d\xi}\right) \quad (13)$$

If we further operate,

$$\int_{z_0}^{z_A}\mu(x,y,\xi)d\xi = -\ln\left(\frac{I^{z_i}(x,y,z_A)}{I^{z_i}(x,y,z_0)}\right) \quad (14)$$

Eq. (14) is a direct relationship between experimental data and projections of the absorption coefficient $\int_{z_A}^{z_0}\mu(x,y,\xi)d\xi$ when $h$ (the PSF) is not an important factor. We recall here that $I^{z_i}(x,y,z_A)$ and $I^{z_i}(x,y,z_0)$ are the intensity in the image plane recorded with and without specimen, respectively. The main consequence of ignoring the point spread function is loosing signal at high frequencies. The importance of this loss will be quantified in the next subsection.

### 2.3.2. Image formation model when the specimen is fully in focus

If the specimen is fully in-focus, then the PSF is only a function of $(x,y)$ but not $z$. Under these conditions, and using the *Second Fundamental Theorem of Calculus*, Eq. (12) may be rewritten as:

$$I^{z_i}(x,y,z_A) = I_g^{z_i}(x,y,z_0)\left(1 - \int_{z_0}^{z_A}\left(\mu(x,y,z)e^{-\int_{z_0}^{z}\mu(x,y,\xi)d\xi}\right)dz\right) \underset{x,y}{\otimes} h(x,y) = I_g^{z_i}(x,y,z_0)\left(e^{-\int_{z_0}^{z_A}\mu(x,y,\xi)d\xi}\right) \underset{x,y}{\otimes} h(x,y) \quad (15)$$

If we further operate,

$$\int_{z_0}^{z_A}\mu(x,y,\xi)d\xi = -\ln\left(\frac{I^{z_i}(x,y,z_A) \underset{x,y}{\otimes} h^{-1}(x,y)}{I^{z_i}(x,y,z_0) \underset{x,y}{\otimes} h^{-1}(x,y)}\right) \quad (16)$$

where, $h^{-1}(x,y)$ is defined as: $h(x,y) \underset{x,y}{\otimes} h^{-1}(x,y) = \delta(x,y)$. For an ideal lens $h$ is the Airy disk and, therefore, $h$ is the squared Airy disk. The Fourier transform of $h$ is a cone shaped function with maximum at the coordinate origin and zero valued for those frequencies greater than $2NA/\lambda$ (where $NA$ is the lens numerical aperture). An estimation of the term $I^{z_i}(x,y,z_A) \underset{x,y}{\otimes} h^{-1}(x,y)$ is beyond the scope of this work but may be delicate at high frequencies where the Fourier transform of $h$ is close to zero. A possible approach to avoid this problem is the use of Wiener filtration as described in Frank (2006). If we compare Eqs. (14) and (16), we may conclude that ignoring the effects of the point spread function (for specimens totally in-focus) is equivalent to a low pass filtration of the results with the filter given by $h$ Fourier transform.

The effects of assuming a constant PSF when it changes along the $z$ axis are more subtle but not unknown. As we rotate the specimen to record a single axis tilt series different specimen features sometimes are in-focus and sometimes out of it. When out of focus they will not contribute to the image and, therefore, we are in a situation similar to the one described in Sorzano et al. (2001) where most of the projections to which a given feature has contributed are generated close to a particular projection direction. When this happens the feature in the reconstruction presents an elongation along the projection direction. Since the different features are in-focus for different angular ranges, the global effect is an elongation of the feature perpendicular to the tilt axis and the radio-vector that joins the feature center and the tilt axis. This effect will become clear when analyzing Fig. 3.

## 2.4. Preprocessing

Preprocessing is usually referred as the initial stage of image processing by which we try to decrease the negative influence in the image quality produced, normally, by a large number of varied and probably unrelated factors, typical of the practical imperfections of concrete image producing parameters. Among these factors, the model of an X-ray microscope as a single lens system needs to be dropped and explicitly take into account the effects of the illumination of the sample at the synchrotron. Currently, our practical experience processing TomoX images comes from our work at Bessy II, and, naturally, this fact necessarily influences our choice of preprocessing operations. Still, many issues are expected to be similar among all three existing microscopes, although some tuning would be required for each setting.

To estimate this nonuniform illumination, typically several images without sample must be taken. These are called *flat fields*. Additionally, the CCD camera acquiring the images has non-zero readings even in the absence of synchrotron light, what is called *dark field*. The dark field as well as the flat field vary over time and for this reason they are measured each time a new data set is recorded. To reduce thermal noise and beam fluctuations, both fields are measured several times.

Additionally, the number of photons arriving to the CCD for a given experimental image (either it is a flat field or a sample field) depends on the intensity of the synchrotron beam, $I_{beam}$, (which

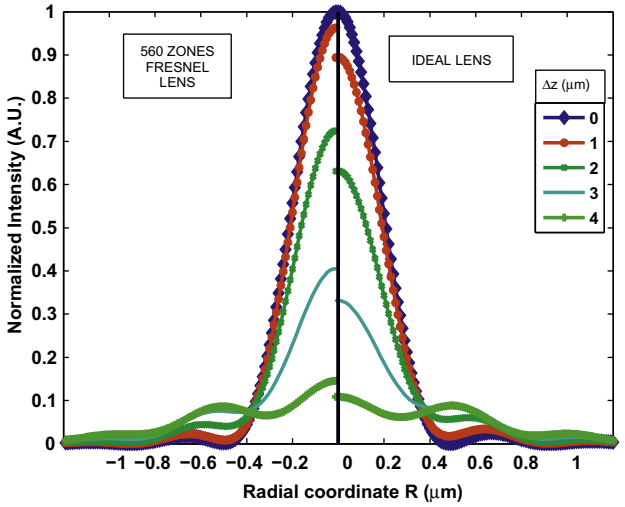


**Fig. 2.** Profiles of the PSF for different defocus ($\delta Z$) for an ideal lens (half-right) and a numerical simulation of a Fresnel zone plate (half-left).

in turn depends on the time elapsed since the last injection and it is one of the synchrotron operating parameters that can be accessed online), the exposure time, $T_{exposure}$, and the slit width, $W_{slit}$ (both parameters can be controlled in the standard X-ray microscope setting).

With all these measurements we propose the following formula to normalize the experimental images in order to compensate for the non-uniform illumination and for the different illumination brightness:

$$I^{(i)}_{normalized} = \frac{\frac{I^{(i)}_{img} - DF^{(avg)}_{experimental}}{I^{(i)}_{beam} T^{(i)}_{exposure} W^{(i)}_{slit}}}{\sum_{f=1}^{N_{FF}} \frac{I^{(f)}_{flatfield} - DF^{(avg)}_{flatfield}}{I^{(f)}_{beam} T^{(f)}_{exposure} W^{(f)}_{slit}}}, \quad (17)$$

where $DF^{(avg)}_{experimental}$ is the average dark field recorded before the experimental tilt series was recorded, $DF^{(avg)}_{flatfield}$ is the average dark field recorded before the flat field measurements were performed, $N_{FF}$ is the number of flatfields used to estimate the average flat field, and $I^{(f)}_{flatfield}$ are the corresponding images, $I^{(f)}_{beam}$, $T^{(f)}_{exposure}$, and $W^{(f)}_{slit}$ represent the synchrotron beam intensity, exposure time and slit width corresponding to the $f$-th measurement of the flat field. Analogously, $I^{(i)}_{experimental}$ represents the $i$-th measurement and $I^{(i)}_{beam}$, $T^{(i)}_{exposure}$, and $W^{(i)}_{slit}$ its acquisition parameters.

Beside this normalization related to the synchrotron and CCD operation, some more preprocessing may be needed to highlight the information content of the tilt series acquired by the X-ray microscope. In particular, spatial bandpass filters (lowpass and highpass filters) may be needed. If we are interested in features with minimum and maximum diameters $d_{min}$ and $d_{max}$, respectively, a bandpass filter with cutoff frequencies $\frac{1}{2d_{max}}$ and $\frac{1}{2d_{min}}$ may be useful. $d_{min}$ is usually set to at least 2 pixels in order to remove rapidly, spatially variant noise. $d_{max}$ is more sample dependent and is usually used to remove uninteresting large features.

In an X-ray microscope the X-ray source is imaged onto the specimen by either a condenser zone plate or a mirror condenser,

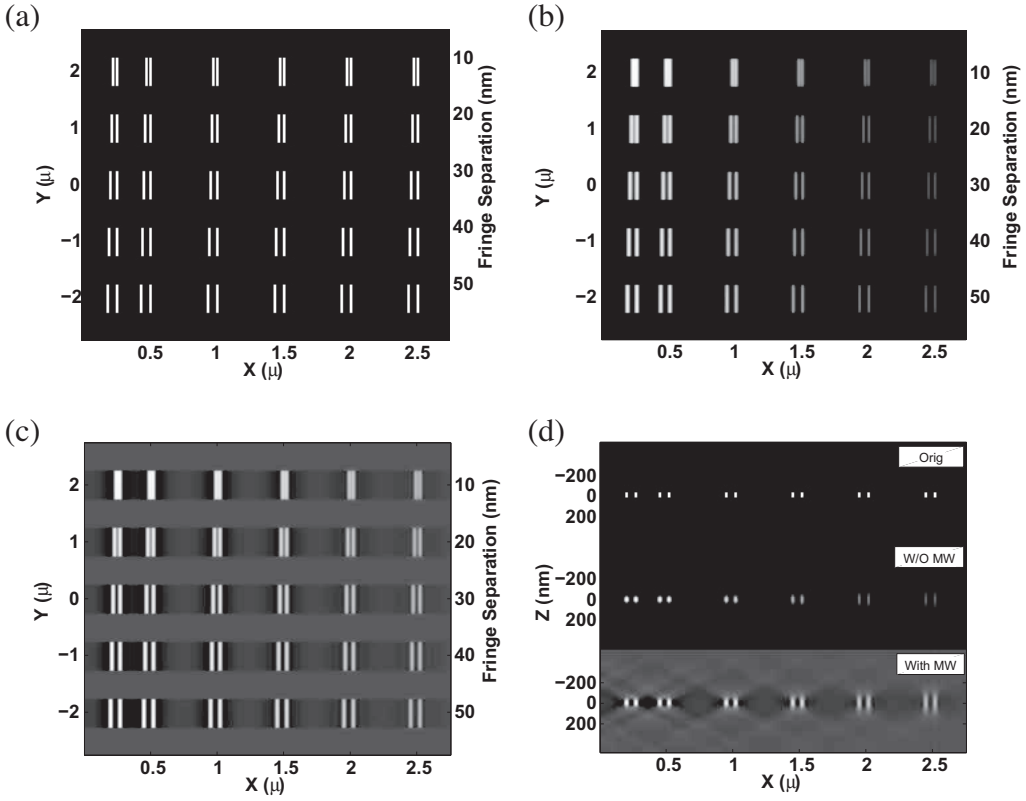


**Fig. 3.** The geometrical phantom has been created using 60 features. Each feature contains a pair of small parallelepipeds (or fringes), 30 of these features are shown in subimage (a). Only two slices in this phantom have pixels with values different from zero, both slices are identical and placed at the volume center. One of these slices is shown in subimage (a), sampling rate is 10 nm/pixel. (a) Phantom central slice perpendicular to $z$ axis (optical axis), since the phantom is symmetric along $x = 0$ plane only half slice is shown. (b) Reconstruction from a complete tilt series (no missing wedge). (c) Reconstruction from a limited set of projections (65 degrees missing wedge). (d) This subfigure presents slices from the three already introduced volumes, but this time they are perpendicular to the $y$ axis (tilt axis) for $y = 40$ nm (tilt axis is parallel to the vertical side of the image). The images at the top, middle and bottom correspond to subimages (a), (b) and (c), respectively.

Q1 Please cite this article in press as: Oton, J., et al. Image formation in cellular X-ray microscopy. J. Struct. Biol. (2012), doi:10.1016/j.jsb.2012.01.006

which is wobbled to provide an even illumination on the sample. An annoying current source of noise is the flickering of illumination produced by this wobbling observed from one image of the tilt series to the next. Considering tilting as a time variable, this flickering is temporal high-frequency information superimposed to the low-frequency variations due to the tilting. The illumination flickering can be removed by temporally low-pass filtering the tilt series. Similarly the spatial filter, the 3D view and corresponding slices of the astrosoma phantom for: (b) cutoff frequency of the lowpass filter can be set to $\frac{1}{2T_{min}}$ filtering the high-frequency information that is not at least in $T_{min}$ tilt images.

## 3. The practical situation in TomoX

So far we have assumed that the PSF of an X-ray microscope is properly approximated by the PSF of a perfect system computed at the focal point. In this subsection we discuss how similar is the PSF of a perfect system to the one made by a Fresnel zone plate. We also explore how the PSF changes for points far away from (i) the object plane that is in focus or (ii) the optical axis.

The answer to the first question is given by Mendoza-Yero et al. (2010) using numeric computation. In this work several point spread functions were computed for points placed on-optical-axis but out-of-focus. The calculations assume a beam line that provides monochromatic X-rays of wavelength $\lambda$ = 2.43 nm and a zone plate with 560 zones and diameter 89.6 μm. Fig. 2 compares the PSF functions obtained by Mendoza-Yero et al. (2010) with the result assuming an ideal lens. As can be seen the general aspect and behavior (for example maxima and minima localization) is very similar although the actual values differ. Therefore, to assume that the PSF of an ideal lens is, indeed, the real PSF is a good first order approximation however, further more quantitative works in TomoX may require to work with PSF calculations in a numerical manner.

The answer to the second question can be obtained from Sypek et al. (2010) using again numerical computation. In this work several PSFs have been simulated for several points at different (i) distances from the optical axis and (ii) defocus. The simulated conditions are identical to the ones described in the previous paragraph. The results prove that the PSF does not change significantly for points closer than 15 μm $t$ the optical axis.

In summary, the results of these calculation support our use of the ideal lens PSF for all points belonging to a typical specimen.

Significant aberrations appears only for points located far away from the optical axis. Therefore, to assume a constant 3D PSF seems to be reasonable in X-ray Tomography.

## 4. Experiments

In order to visualize the importance of the depth of focus in TomoX, several experiments have been made. The first set of experiments uses a phantom made from simple geometrical structures (fringes) which is fully described in Fig. 3. These experiments were designed to find the resolution limits induced by the limited depth of focus. A simple phantom was selected since reconstruction artifacts are more clearly identifiable in these structures. For the second set of experiments we used a more biologically oriented phantom inspired in the work on *Candida albicans* published by Uchida et al. (2009). This phantom was made using two copies of *C. albicans*, the first copy was placed at the volume center while the second one was divided in two halves and placed along the optical axis before and after the central motive (see Fig. 5 for details). A control phantom was also created consisting in a single copy of *C. albicans*. Since the reconstructions of the overlapping



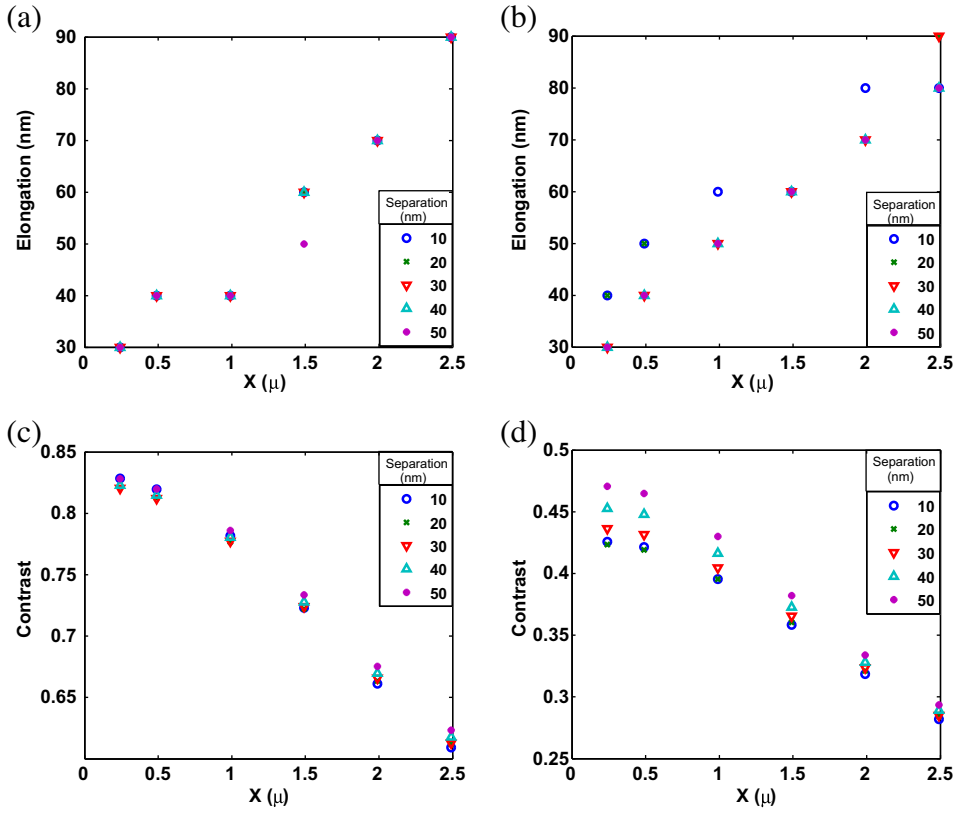


**Fig. 4.** Plots showing elongation (top) and contrast (bottom) for the geometrical phantom reconstructed from a tilt series without (left) and with (right) missing wedge. Results for different fringe separations are provided.

sections of these two later phantoms were identical we will report only on the larger phantom.

### 4.1. Projection generation

Using the Xmipp image processing package (Sorzano et al., 2004) projection images (as described by Eq. (12)) were created simulating the effect introduced by an X-ray microscope with a Fresnel zone plate of 560 zones and 40 nm. outer zone width (depth of focus 2.63 μm). The data collection geometry was single axis with one degree steps; the tilt axis is the *y* axis. Two data sets were generated one with missing wedge between ±65 degrees and another without missing wedge. The different projection sets were reconstructed with standard 3DEM software which assumes that the whole volume is in-focus, no attempt to correct for the PSF was made.

#### 4.1.1. Geometrical phantom

Geometrical phantom reconstructions are presented in Fig. 3, where we present slices of the 3D phantom perpendicular to different axis. In Fig. 3(a) we show a slice of the original phantom, the tilt axis is along the *y* axis, on the left hand side of the figure. Fringes are spaced along *x*, extending several pixels parallel to the *y* axis and only 2 pixels along *z*. The spacing within each set of fringes is shown on the right hand side of the figure. In Fig. 3(b) and 3(c) we note a loss of contrast as we move away from the tilt axis, being more pronounced in the missing wedge case. The general decrease of contrast in the case of missing wedge is a known phenomenon in other tomographic microscopies. However, the change in contrast in the direction perpendicular to the tilt axis is due to the relatively limited depth of focus of TomoX. In this way, fringes far away from the tilt axis move out of focus as we rotate the specimen, resulting in a weaker contribution to the reconstruction.

Fig. 3(d) presents a section through the *zx* plane for the initial phantom, the reconstruction without missing wedge, and the one with missing wedge for a fringe separation of 40 nm. The point to remark in this figure is that there is a quite noticeable elongation along the *z* direction, and that it increases as we move away from the tilt axis. In general, the elongation will be perpendicular to the tilt axis and the radio-vector that joins the feature center and the tilt axis (provided that the plane in-focus is $z = 0$). Since in our experiments the tilt axis lays along the *y* axis and the feature centers are in the $z = 0$ plane, the radio vector is parallel to the *x* axis and the elongation is along the *z* axis. Again, these effects are typical of a limited depth of focus, as it happens in TomoX. If the whole specimen were in focus, the elongation would only be along the *z* axis, and it would not depend on the distance to the tilt axis.

In order to quantify the importance of the different effects, we have measured the contrast and elongation of fringe features in the different images. Contrast is defined by plotting the intensity at the feature center along the *x* axis, then computing its maximum value (in the area defined by the feature white bars) and minimum value (in the area between the white bars) and calculating the magnitude $\frac{max - min}{max + min}$. Elongation is defined by plotting the first white bar of a fringe along the *z* axis, computing its maximum value and then finding the first two points before and after the white bar center with values lower than $\frac{max}{e}$ (where *e* is the Euler number). The distance between these two points is the elongation.

Elongation and contrast have been recorded for the two data sets described above, one with missing wedge between ±65 degrees and another without missing wedge. Results show (see plots Fig. 4(a and b)) how, for the phantom used in this experiment, the elongation (along the *z* axis) increases from 30 to 45 nm close to the tilt axis (while ideally it should be 20 nm) to 80 nm as we move 2.5 μm from the center. The effects in the *xy* plane (see plots Fig. 4(c and d)) shows how the contrast decreases as we move from the tilt axis and drops about a 20% close to volume edge.

A very noticeable result shown in Fig. 3 is that contrast degradation and elongation are qualitatively very similar without and with missing wedge. This non-expected behavior indicates that effects due to the limited depth of focus may be more noticeable that otherwise expected missing wedge degradations. In other words, TomoX, because of its relatively limited depth of focus, indeed presents important particularities as compared, for instance, to electron tomography.



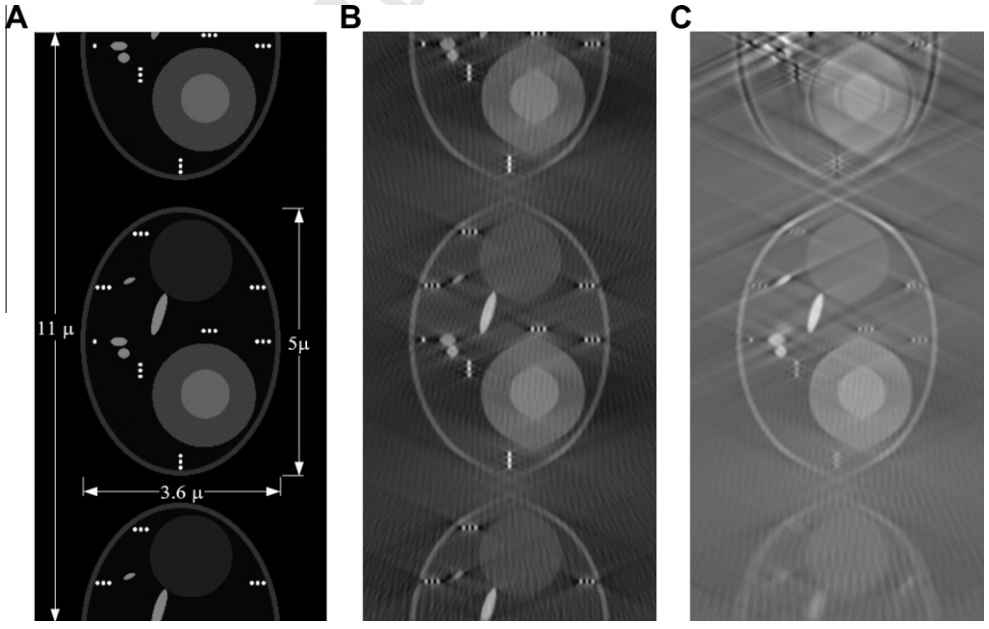


**Fig. 5.** *Candida*-inspired phantom, created using two copies of *Candida albicans* placed along the optical axis *z* (a) central slice of the reference phantom defined by the plane $y = 0$, (b) reconstruction from ideal data filtered to the X-ray microscope cut-off frequency and (c) reconstruction from X-ray microscope simulated data. Geometry collection: tilt axis with 65 degrees missing wedge (tilt axis is perpendicular to the image).

Q1 Please cite this article in press as: Oton, J., et al. Image formation in cellular X-ray microscopy. J. Struct. Biol. (2012), doi:10.1016/j.jsb.2012.01.006

#### 4.1.2. Candida phantoms

*Candida phantom* is shown in Fig. 5. Subimages 5(a–c) shows the same slice perpendicular to the tilt axis for: (a) the original phantom, (b) a reconstruction from ideal projections filtered to the X-ray microscope cut-off frequency and (c) a reconstruction with missing wedge from projections created following the X-ray microscope image formation model. As we move from the tilt axis (placed at the image center) the different phantom features became more and more blurred. At defocus values greater than 3 μs (moving towards the lens) contrast inversion appears close to the feature borders. The situation changes if we move far away from the lens. In this case, again at about 3 μs, the contrast decays and the features became very blurry. This asymmetric behavior is due to the fact that the PSF is not a spatially symmetric function (except when expressed as a function of diopters instead of space) and it changes slower as we move from the lens.

In summary, for the microscope simulated in this work, specimens with sizes equal or less than 5 μs are only partially affected by the TomoX limited depth of focus while bigger specimens will perform poorly for those details placed far away (3 μs) from the in-focus plane.

## 5. Discussion

In this work we have followed a systematic approach to the study of the image formation process in a cellular X-ray microscope at the task of visualizing objects of several microns and within the approximation of incoherent illumination. This study is to be considered an initial contribution to the field, that should be followed by more realistic illumination models, including partially coherent illumination, as well as the modification of reconstruction algorithms so that they incorporate at their core the so derived image formation model.

We have studied the illumination of the sample from images obtained at Bessy II, proposing a method for image normalization that aims at partially compensating for the unstable illumination, as described in Section 2.4. We have studied in detail the core of the image formation process, deriving a formula modeling in quantitative terms the effects of variable depth of focus and absorption in the final images under our stated approximations. The main conclusion of the latter derivation and the provided simulated images experiments is to start providing more accurate bases onto which to derive new tomographic algorithms for thick (about 10 μm or thicker) biological specimens.

It is interesting to consider that for thin specimens this work supports the standard approach in TomoX field, that is, it is valid to process the data ignoring the microscope PSF if, and here we depart from standard practice, the reconstruction is followed by the sharpening high resolution filter described at Section 2.3.2. A similar – in spirit – approach is followed in the electron microscopy field with the so-called B-Factor value (Rosenthal and Henderson, 2003). For thick specimens new developments are needed that should address the incorporation of the proper image formation process described in Eq. (12) in the reconstruction algorithms.

## Acknowledgments

This work was funded by the Spanish Ministerio de Ciencia e Innovación (CSD2006-0023, BFU2009-09331, BIO2010-16566, ACI2009-1022, ACI2010-1088). We give special thanks to Stephan Heim, Ph.D. student at Bessy Synchrotron, for his contributions to the Preprocessing section. C.O. Sorzano is a recipient of a *Ramón y Cajal* fellowship financed by the European Social Fund and the Ministerio de Educación y Ciencia. Joaquin Oton is supported by a Juan de la Cierva Research Fellowship from the Ministerio de Ciencia e Innovación.

## Appendix A

In this appendix we make a more detailed derivation of Eq. (8) from Eq. (7). We follow the general guide lines given by Goodman (1996) Section 6.1.3.

$$
\begin{aligned}
I^{z_i}(x,y,z_a+\Delta z_a) &= \langle U^{z_i}(x,y,z_a+\Delta z_a)U^{z_i*}(x,y,z_a+\Delta z_a)\rangle \\
&=< \iint\iint U^{z_i}(\xi,\eta,z_a+\Delta z_a)\hat{h}(x-\xi,y-\eta,D(z_a+\Delta z_a,z_i))d\xi d\eta \\
&\quad U^{z_{i*}}(\xi',\eta',z_a+\Delta z_a)\hat{h}^*(x-\xi',y-\eta',D(z_a+\Delta z_a,z_i))d\xi' d\eta' > \\
&=< \iint\iint (1-\tilde{\mu}^R(\xi,\eta,z_a)\Delta z_a - j\tilde{\mu}^I(\xi,\eta,z_a)\Delta z_a) \\
&\quad U_g^{z_i}(\xi,\eta,z_a+\Delta z_a)\hat{h}(x-\xi,y-\eta,D(z_a+\Delta z_a,z_i)) \\
&\quad (1-\tilde{\mu}^R(\xi',\eta',z_a)\Delta z_a + j\tilde{\mu}^I(\xi',\eta',z_a)\Delta z_a) \\
&\quad U_g^{z_{i*}}(\xi',\eta',z_a+\Delta z_a)\hat{h}^*(x-\xi',y-\eta',D(z_a+\Delta z_a,z_i)) \\
&\quad d\xi d\eta d\xi' d\eta' > \\
&=< \iint\iint (1-\tilde{\mu}^R(\xi,\eta,z_a)\Delta z_a - j\tilde{\mu}^I(\xi,\eta,z_a)\Delta z_a) \\
&\quad (1-\tilde{\mu}^R(\xi',\eta',z_a)\Delta z_a + j\tilde{\mu}^I(\xi',\eta',z_a)\Delta z_a) \\
&\quad \widehat{U_g^{z_i}(\xi,\eta,z_a+\Delta z_a)U_g^{z_{i*}}(\xi',\eta',z_a+\Delta z_a)} \\
&\quad \hat{h}(x-\xi,y-\eta,D(z_a+\Delta z_a,z_i))\hat{h}^*(x-\xi',y-\eta',D(z_a+\Delta z_a,z_i)) \\
&\quad d\xi d\eta d\xi' d\eta' >
\end{aligned}
$$

To calculate the image intensity, we must time average the instantaneous intensity. Due to the fact that the detector integration time is long compared with the bandwidth many terms simplify as shown in Goodman (1996) Eqs. (6.7)–(6.15).

$$
\begin{aligned}
&= \iint (1-\tilde{\mu}^R(\xi,\eta,z_a)\Delta z_a + j\tilde{\mu}^I(\xi,\eta,z_a)\Delta z_a) \\
&\quad (1-\tilde{\mu}^R(\xi,\eta,z_a)\Delta z_a - j\tilde{\mu}^I(\xi,\eta,z_a)\Delta z_a) \\
&\quad U_g^{z^i}(\xi,\eta,z_a)U_g^{z^{i*}}(\xi,\eta,z_a+\Delta z_a) \\
&\quad \hat{h}(x-\xi,y-\eta,D(z_a+\Delta z_a,z_i))\hat{h}^*(x-\xi,y-\eta,D(z_a+\Delta z_a,z_i))d\xi d\eta \\
&= \iint (1-\tilde{\mu}^R(\xi,\eta,z_a)\Delta z_a - j\tilde{\mu}^I(\xi,\eta,z_a) \\
&\quad \Delta z_a) - \tilde{\mu}^R(\xi,\eta,z_a)\Delta z_a + j\tilde{\mu}^I(\xi,\eta,z_a)\Delta z_a + O^2(\Delta z_a))(I_g^{z^i}(\xi,\eta,z_a)) \\
&\quad h(x-\xi,y-\eta,D(z_a+\Delta z_a,z_i))d\xi d\eta \\
&\approx (1-\mu(x,y,z_a)\Delta z_a)I_g^{z^i}(x,y,z_a) \underset{x,y}{\otimes} h(x,y,D(z_a+\Delta z_a,z_i))
\end{aligned}
$$

## References

Agard, D., Hiraoka, Y., Shaw, P., Sedat, J., 1989. Fluorescence microscopy in three dimensions. Fluorescence microscopy of living cells in culture. Methods Cell Biol. 30, 353–377.

Attwood, D., 2007. Soft X-Rays and Extreme Ultraviolet Radiation: Principles and Applications, first ed. Cambridge University Press, New York, NY, USA.

Bertilson, M., von Hofsten, O., Hertz, H.M., Vogt, U., 2011. Numerical model for tomographic image formation in transmission X-ray microscopy. Optics Express 19, 11578–11583.

Carrascosa, J.L., Chichon, F.J., Pereiro, E., Rodriguez, M.J., Fernandez, J.J., Esteban, M., Heim, S., Guttmann, P., Schneider, G., 2009. Cryo-X-ray tomography of vaccinia virus membranes and inner compartments. J. Struct. Biol. 168, 234–239.

Dey, N., Boucher, A., Thonnat, M., 2002. Image formation model of a 3D translucent object observed in light microscopy. In: Proceedings. International Conference on Image Processing, Rochester, NY, USA. pp. II-469–II-472.

Frank, J., 2006. Three Dimensional Electron Microscopy of Macromolecular Assemblies. Oxford University Press, New York.

Frank, J., Radermacher, M., Penczek, P., Zhu, J., Li, Y., Ladjadj, M., Leith, A., 1996. SPIDER and WEB: processing and visualization of images in 3D electron microscopy and related fields. J. Struct. Biol. 116, 190–199.

Goodman, J.W., 1996. Introduction to Fourier Optics. McGraw-Hill, New York.

Gu, W., Etkin, L.D., Le Gros, M.A., Larabell, C.A., 2007. X-ray tomography of *Schizosaccharomyces pombe*. Differentiation 75, 529–535.
Hanssen, E., Knoechel, C., Dearnley, M., Dixon, M.W., Le Gros, M., Larabell, C., Tilley, L., 2011. Soft X-ray microscopy analysis of cell volume and hemoglobin content in erythrocytes infected with asexual and sexual stages of *Plasmodium falciparum*. J. Struct. Biol..
von Hofsten, O., Takman, P.A.C., Vogt, U., 2007. Simulation of partially coherent image formation in a compact soft X-ray microscope. Ultramicroscopy 107, 604–609, PMID: 17261350.
Howells, M., Jacobsen, C., Warwick, T., 2007. Principles and applications of zone plate X-ray microscopes. In: Hawkes, P., Spence, J. (Eds.), Science in Microscopy, pp. 835–926.
Jacobsen, C., 1992. Making soft X-ray microscopy harder: considerations for sub-0.1 micron resolution imaging at 4a° wavelengths, In: Michette, A.G., Morrison, G.R., Buckley, C.J. (Eds.), X-ray Microscopy III. Volume 67 of Springer Series in Optical Sciences. Springer-Verlag, Berlin, pp. 274–277.
Kirz, J., Jacobsen, C., Howells, M., 1995. Soft X-ray microscopes and their biological applications. Q. Rev. Biophys. 28, 33–130.
Kremer, J.R., Mastronarde, D.N., McIntosh, J.R., 1996. Computer visualization of three-dimensional image data using IMOD. J. Struct. Biol. 116, 71–76.
Larabell, C.A., Le Gros, M.A., 2004. X-ray tomography generates 3-D reconstructions of the yeast, *Saccharomyces cerevisiae*, at 60-nm resolution. Mol. Biol. Cell 15, 957–962.
Le Gros, M.A., McDermott, G., Larabell, C.A., 2005. X-ray tomography of whole cells. Curr. Opin. Struct. Biol. 15, 593–600.
Mendoza-Yero, O., Mínguez-Vega, G., Navarro, R., Lancis, J., Climent, V., 2010. PSF analysis of nanometric fresnel zone plates. In: Proceeding of the EOS Topical Meeting on Diffractive Optics, Koli, Finland.
Mielenz, K.D., 1999. On the diffraction limit for lensless imaging. J. Res. NIST 104, 479–485.
Parkinson, D.Y., McDermott, G., Etkin, L.D., Le Gros, M.A., Larabell, C.A., 2008. Quantitative 3-D imaging of eukaryotic cells using soft X-ray tomography. J. Struct. Biol. 162, 380–386.
Rosenthal, P.B., Henderson, R., 2003. Optimal determination of particle orientation, absolute hand, and contrast loss in single-particle electron cryomicroscopy. J. Mol. Biol. 333, 721–745.
Rudolph, D., Schmahl, G., Niemann, B., 1990. Amplitude and phase contrast in X-ray microscopy. In: Duke, P.J., Michette, A.G. (Eds.), Mod. Microsc.. Plenum, New York, pp. 59–67.
Schmahl, G., Rudolph, D., 1987. Proposal for a phase contrast X-ray microscope. In: Cheng, P., Jan, G. (Eds.), X-ray Microscopy. Springer-Verlag, Berlin, pp. 231–238.
Schneider, G., 1998. Cryo X-ray microscopy with high spatial resolution in amplitude and phase contrast. Ultramicroscopy 75, 85–104.
Schneider, G., Guttmann, P., Heim, S., Rehbein, S., Mueller, F., Nagashima, K., Heymann, J.B., Muller, W.G., McNally, J.G., 2010. Three-dimensional cellular ultrastructure resolved by X-ray microscopy. Nat. Methods 7, 985–987.
Sorzano, C.O.S., Marabini, R., Boisset, N., Rietzel, E., Schröder, R., Herman, G.T., Carazo, J.M., 2001. The effect of overabundant projection directions on 3D reconstruction algorithms. J. Struct. Biol. 113, 108–118.
Sorzano, C.O.S., Marabini, R., Velázquez-Muriel, J., Bilbao-Castro, J.R., Scheres, S.H.W., Carazo, J.M., Pascual-Montano, A., 2004. XMIPP: a new generation of an open-source image processing package for electron microscopy. J. Struct. Biol. 148, 194–204.
Sypek, M., Makowski, M., Kolodziejczyk, A., Navarro, R., 2010. Calculations of PSF functions for X-ray zone plates with high number of zones. In: Proceeding of the EOS Topical Meeting on Diffractive Optics, Koli, Finland.
Thieme, J., Schneider, G., Knochel, C., 2003. X-ray tomography of a microhabitat of bacteria and other soil colloids with sub-100 nm resolution. Micron 34, 339–344.
Uchida, M., McDermott, G., Wetzler, M., Le Gros, M.A., Myllys, M., Knoechel, C., Barron, A.E., Larabell, C.A., 2009. Soft X-ray tomography of phenotypic switching and the cellular response to antifungal peptoids in *Candida albicans*. Proc. Natl. Acad. Sci. USA 106, 19375–19380.
Weiss, D., Schneider, G., Niemann, B., Guttmann, P., Rudolph, D., Schmahl, G., 2000a. Computed tomography of cryogenic biological specimens based on X-ray microscopic images. Ultramicroscopy 84, 185–197.
Weiss, D., Schneider, G., Niemann, B., Guttmann, P., Rudolph, D., Schmahl, G., 2000b. Computed tomography of cryogenic biological specimens based on X-ray microscopic images. Ultramicroscopy 84, 185–197 (PMID: 10945329).
Wolter, H., 1952. Spiegelsysteme streifenden Einfalls als abbildende Optiken für Röntgenstrahlen. Ann. Phys. 445, 94–114.